

V. Lawlor¹

Department of Eco-Energy,
Upper Austrian University of Applied Science,
A-4600 Wels, Austria;
Department of Manufacturing and
Mechanical Engineering,
Dublin City University,
Dublin 9, Ireland
e-mail: vlawlor@gmail.com

K. Klein

eZelleron GmbH,
Collenbuschstr. 22,
01324 Dresden, Germany

C. Hochenauer

S. Griesser

Department of Eco-Energy,
Upper Austrian University of Applied Science,
A-4600 Wels, Austria

S. Kuehn

eZelleron GmbH,
Collenbuschstr. 22,
01324 Dresden, Germany

A.-G. Olabi

Department of Manufacturing and
Mechanical Engineering,
Dublin City University,
Dublin 9, Ireland

S. Cordiner

Dipartimento di Ingegneria Meccanica,
Università di Roma Tor Vergata,
00133 Rome, Italy

G. Buchinger

Department of Eco-Energy,
Upper Austrian University of Applied Science,
A-4600 Wels, Austria

Experimental and Numerical Study of Various MT-SOFC Flow Manifold Techniques: Single MT-SOFC Analysis

Standard anode supported micro tubular-solid oxide fuel cell (MT-SOFC) stacks may provide the oxidant, in relation to the fuel, in three different manifold regimes. Firstly, “co-flow” involves oxidant outside the MT-SOFC flowing co-linearly in relation to the fuel inside. Secondly, “counter flow” involves oxidant outside the MT-SOFC flowing counter-linearly in relation to the fuel inside the MT-SOFC. Finally, “cross-flow” involves the oxidant outside the MT-SOFC flowing perpendicular to the fuel flow inside the MT-SOFC. In order to examine the effect of manifold technique on MT-SOFC performance, a combination of numerical simulation and experimental measurements was performed. Furthermore, the cathode current tap location, in relation to the fuel flow, was also studied. It was found that the oxidant manifold and the location of the cathode current collection point on the MT-SOFC tested and modeled had negligible effect on the MT-SOFC’s electrical and thermal performance. In this study, a single MT-SOFC was studied in order to establish the measurement technique and numerical simulation implementation as a prerequisite before further test involving a 7 cell MT-SOFC stack.

[DOI: 10.1115/1.4023216]

1 Introduction

Solid oxide fuel cells (SOFCs) are becoming ever more relevant as a means of converting fuels to electricity. The fact that they can be fuelled with hydrocarbon fuels, require no precious materials in their production, and now, with smaller versions, can be rapidly heated to operational temperature makes them a viable alternative to traditional energy conversion systems. SOFCs produce excess heat that may thermally self sustain the stack, drive peripheral electricity generation devices or reformers, or heat water. SOFC stacks have been reported to provide as much as 85% fuel utilization [1,2]. Simulation results of Chan et al. [3] show that their SOFC-gas turbine power system could achieve a net electrical

efficiency of better than 60% and a system efficiency (including waste heat recovery for steam generation) of better than 80%. Other reports of such high efficiencies for SOFC gas turbine systems can be found in Refs. [4–10]. Sidwell and Coors [11] have shown that peak electrical efficiency is a compromise between fuel utilization and operating voltage, which act in opposition to each other. They concluded that it is possible to exceed 60% electrical efficiency in internally reforming SOFCs. The maximum reported electrical conversion efficiency for a SOFC system (3.1 kW) has been reported as 59% (direct current (DC), lower heating value (LHV)) [12], which it is claimed reached the world’s highest level at the time of publication (2009).

The MT-SOFC is a much smaller version of the standard planar and tubular SOFC systems. Specifically for MT-SOFCs, Howe et al. [13], in a recent review paper, have shown that MT-SOFC fuel utilization in the literature averages from 50% to a maximum of 79%. Normally, MT-SOFCs are considered for small scale, in the order of W to kW, stationary power generation, and indeed

¹Corresponding author.

Contributed by the Advanced Energy Systems Division of ASME for publication in the JOURNAL OF FUEL CELL SCIENCE AND TECHNOLOGY. Manuscript received November 24, 2011; final manuscript received April 14, 2012; published online January 15, 2013. Assoc. Editor: Masashi Mori.

mobile power provision, while the larger SOFCs have been envisaged for large scale kW to MW stationary power systems. For example, larger SOFCs have been envisaged for combined heat and power (CHP) in residential areas [9,14,15].

The MT-SOFC is an evolution of the standard SOFC that has added resilience against thermal shocks, which allows a fast start-up and a high power per volume [16]. Originally, Kendall demonstrated with his 1000 cell stack that MT-SOFCs could be heated up to their operational temperature of 850 °C at a rate of 200 °C/min [17]. In 1996, Kendall also set up the first MT-SOFC company called Adelan (UK) Ltd. With these Adelan cells, Bujalski et al. [16] showed that MT-SOFCs could be consistently ramped to operational temperature at a rate of 4000 °C/min without any MT-SOFC structural damage or power degradation. This would mean that the MT-SOFCs would be at their operational temperature after 12 s, which is only a little slower than reciprocating engine. Of course, it should be noted that the apparatus used in order to perform these tests was specifically designed for single cell tests and a stack of these MT-SOFCs will have its heating up and cooling down rates further limited by the thermal stresses induced by the reactor housing and seals. A honeycomb structured MT-SOFC stack with power density of 1 W/cm³ [18] has been shown to be operational within 100 s [19]. Such a stack would fit perfectly to the estimated system predictions of Lin and Hong [20], whereby their system, without the stack thermal mechanical consideration being of concern, stated a 100 s time for their modeled system to reach operation. An “always on” SOFC is being envisaged as an alternative to the previously mentioned approach in order to constantly charge batteries in electrical vehicles [21], thus avoiding thermal cycling issues.

Very recently, Du et al. [22] showed with their MT-SOFCs (Nano-Dynamics USA, Inc.), regardless of single MT-SOFC tests or stack tests, that thermal cycling of their cells did not cause any MT-SOFC degradation. They recommended that their stacks can be heated up at rates of 550 °C/min and that their MT-SOFCs produced the normal operational power as soon as it reached the operational temperature of 800 °C. Notably, their single MT-SOFC tests just involved placing the cells into preheated ovens for heating up and simply removing them for cooling down.

It would seem that the MT-SOFC has many beneficial characteristics that the larger SOFC types do not adhere to, with specific reference to their high volumetric power density and thermal shock resistance. In 1995, Penner et al. [23] mentioned in a paper dealing with the commercialization of SOFCs, among many other improvements, that increasing tubular SOFCs power density was key to their marketplace potential. The MT-SOFC is not mentioned in this paper, but its power density is much greater than the larger SOFC tube type. Lutsey et al. [24] have shown that small SOFCs are ideally suited for auxiliary power unit (APU) use. For example, in long haul trucks when the SOFC is used during idling times. In their quantitative market potential and cost-effectiveness study regarding an SOFC as a truck APU, they concluded that as SOFC technology approaches \$800 per net kW (in 2015), such a product would become cost efficient for haulers with a two year payback time. However, a recent independent study by the U.S. Department Of Energy [25] for other SOFC systems has suggested a figure of 1000–3000 dollars/kW for 2015, which may scuttle this cost efficiency prognosis. Moreover, the MT-SOFC is the ideal candidate for such niche markets because it has a rapid start-up capability and high shock resistance.

Furthermore, unlike other technologies such as polymer electrolyte membrane fuel cells (PEMFCs), batteries and combustion engines' MT-SOFCs and SOFCs have no track record in mobile applications. Of extreme concern will be the stack mechanical stability, whereby small failures such as cracks in SOFC systems are serious. Therefore, this current study is also important in order to provide qualitative and quantitative data regarding possible thermal gradients across the MT-SOFC and sealing areas.

A substantial MT-SOFC range of literature is available to the field, both with regard to modeling works and experimental work.

For a detailed analysis of modeling and experimental activities up to 2009, the reader is referred to Refs. [26–28].

The aim of this study was to examine several oxidant and fuel manifold techniques and their thermally induced effect on MT-SOFC performance. The MT-SOFCs used in this study were fundamentally small tubes having a 2.7 mm outer diameter and a 3.5 cm cathode length. A tubular gas tight electrolyte separates a fuel on the anode side (inside the tube) and an oxidant on the cathode side (outside the tube) in order to supply redox electrochemistry with reactants. As far as the authors are aware, there has been no study that investigates the oxidant manifold regime in the scientific literature, specifically for MT-SOFCs. Comparisons in the literature of the co-, counter-, and cross-flow methods may only be found for big SOFC tubes and planar cells. For example, Recknagle et al. [29] examined the effects of these three different methods on a planar SOFC with a validated electrochemical code and combined it with computational fluid dynamics (CFD) software.

The role of the flow regime between and around MT-SOFCs within arrays and also through them internally is a very important consideration in an MT-SOFC stack design. This issue has been addressed to some degree by several authors. For example, recently Serincan et al. [30] have investigated the steady state behavior of an MT-SOFC inside an oven in a very comprehensive and enlightening 2D model. The fuel temperature in the anode increased by about 110 °C between open circuit voltage (OCV) and 0.2 V. Such a temperature response should affect the system response. Furthermore, they found temperature gradient field ranges of 18 and 40 °C on the cathode and anode sides. In their model, the electrolyte temperature is slightly higher than the electrodes', ranging from 0.1 °C at OCV to 0.9 °C at 0.2 V. This is probably because of the reactions taking place in that vicinity. For further information on CFD modeling of MT-SOFCs, the reader is pointed to Refs. [31–33].

The results of this initial study will establish the capability of a combined experimental method using a specially designed apparatus, miniature thermocouples and CFD analysis, in order to qualitatively and quantitatively establish the effects of a single MT-SOFC's performance as a function of oxidant manifold regime. Also, the cathode current tap location effect on MT-SOFC performance was also considered. The results will clearly show realistic temperature measurements via the thermocouple readings and realistic electrical performance measurements via I/V curves. This data was compared with CFD simulation predictions in order to predict, in detail, what is occurring inside the test chamber, which cannot be easily observed visually or using an infrared detection apparatus. The lessons learned from this study will be a valuable asset when attempting to perform the same measurements within a seven cell bundle within the same apparatus. Moreover, the information learnt from this study will be very important in order to understand the effects inside a MT-SOFC stack depending on the flow regime.

2 Materials and Methods

2.1 Experimental Apparatus. The experimental apparatus, as seen in Fig. 1, was constructed of Crofer 22APU and Conicro 5010W both from ThyssenKrupp AG Germany, heating bulbs (Phillips GmbH, Germany), and top insulation, not shown, Ultra board (Porextherm GmbH, Germany) bottom insulation (regular porous concrete block). The testing apparatus heating was regulated by thermocouples placed in the testing chamber that touched the top and bottom walls. Two further thermocouples were placed on the testing chamber side of the cross flow air in the diffuser. Each oxidant inlet pipe also had thermocouples placed inside. These were used in order to monitor the temperature at various locations within the inlet/outlet pipes. All thermocouples were covered at their tips with blobs of chimney and oven sealant (UHU GmbH, Germany) in order to minimize errors due to

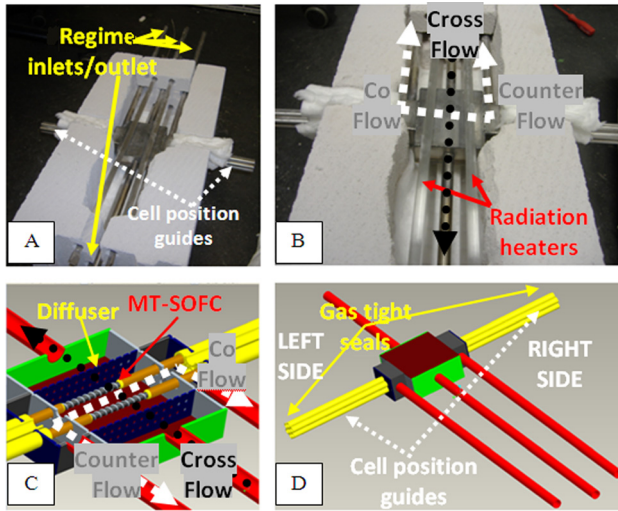


Fig. 1 (a) A photograph showing the experimental apparatus. (b) A photograph showing the heating mechanism and indication of oxidant gas flow direction. (c) A CAD drawing showing the layout inside the apparatus. (d) A CAD drawing showing the cell guides and location of gas tight seals.

radiation reflection and emission effects. I/V curve measurements were made using a Bio-Logic (sas Fr) VSP potentiostat system and VMP 3B 5 A booster. The rated potential measurement error was 0.1% full scale range (FSR) and rated DC current measurement error was 0.2% FSR.

Figure 1(a) solid arrows show the oxidant inlet and outlet with the pipe ends positioned 40cm away from the apparatus in order to keep the plastic air inlet pipes that were connected to them below their melting point. The broken arrows show the location of the MT-SOFC position guides. The ceramic MT-SOFC fuel manifolds and MT-SOFCs were guided into the testing chamber through these larger steel pipes. Figures 1(b) and 1(c) white, broken arrow show the co- and counter-flow manifold techniques, and the black, dotted arrow shows the cross flow technique. Two MT-SOFCs are shown in Fig. 1(c) in order to display that this apparatus was designed for a seven cell stack. The MT-SOFC under test was located in the middle cell guide. Finally, Fig. 1(d) yellow, whole arrows show the location of the gas tight seals made between the apparatus and the ceramic MT-SOFC fuel manifolds. For these single MT-SOFC tests all other guide pipes were blocked using high temperature silicone. In order to create the various oxidant flow regimes, one of the apparatus's oxidant feed/exhaust pipes was used as the oxidant inlet and another as the oxidant outlet. The remaining two pipes were blocked in order for the oxidant to be driven out the decided oxidant outlet pipe.

The equipment used to make the thermal measurements was thermocouples (Type K and LCD display unit TC Direct, UK) (Accuracy $\pm 1.5\%$ or about 10 K at 1023 K). All the thermocouples used were tested by observing the phase transition of solid aluminum to liquid at 933 K and silver at 1235 K. Furthermore, a LabVIEW (NI Corp.) DAQ and control program was written in order to perform the experiments. Small errors in the thermocouple readings were accounted for in the LabVIEW code in order to provide immediately comparable readings. The thermocouple locations on the MT-SOFC cathode are shown in Fig. 2. The thermocouples used in order to measure the cathode temperature were 0.25 mm diameter miniature thermocouples provided by TC Direct, UK. In addition to the silver wire seen in Fig. 2, silver paste was used to form rings and strips on the cathode, seen also in Fig. 3, see Sec. 3.1. In Fig. 2 "H₂ + in" means that the cathode current tap (location where the electrons return to the cathode current collector on the cathode) was located at the MT-SOFC fuel inlet side. "H₂ + out" means that the cathode current tap was located at the fuel outlet side of the MT-SOFC. Note that 25 °C and 101,325 Pa used for the calculation of normalized volume flow rates is stated in this study. Furthermore, the apparatus top and bottom wall temperatures (inside the apparatus) were maintained at 1050 K. This resulted in a passive (under OCV conditions) MT-SOFC temperature of 1046 K.

3 Theory and Calculation

3.1 Theory. A commercially available CFD modeling software [34] with an additional electrochemical module [35] was used in order to simulate the different manifold designs addressed in this study. The SOFC module predicts the electrochemical performance of the MT-SOFC and is built upon the following principles and equations.

- Fluid flow, heat transfer, and the mass transfer in the flow channels and in the porous anode and cathode electrodes are accounted for.
- The current and the potential field in the porous electrodes and in the solid conducting regions are accounted for.
- The electrochemical reactions that take place at the electrolyte/electrode/gaseous species interface are accounted for.

Since the local Nernst potential depends upon the fuel and oxidant composition at the three phase boundary locations, an SOFC's current density distribution and the transport behavior are locally dependent. Additionally, the activation and limit losses coupled to the electrolyte are a function of the current density. In the electrochemical module chosen for this study [35], either side of the SOFC's electrolyte was partitioned by local potential difference. The Nernst potential, the ohmic loss within in the electrolyte, and the activation losses associated at the electrode/electrolyte interfaces provided the terms required in order to calculate this potential difference. The CFD-SOFC module chosen assumed an

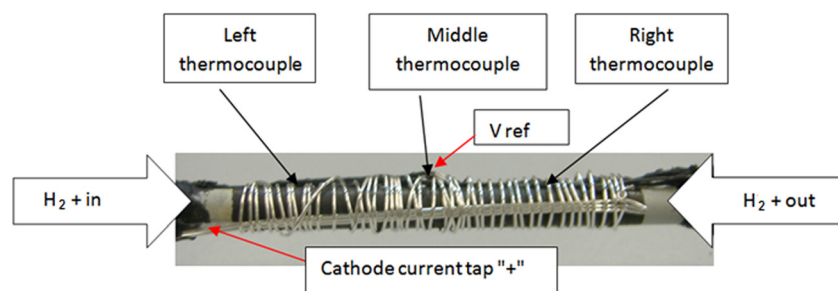


Fig. 2 Location of thermocouples and current collector on the MT-SOFC used in the experimental apparatus. Note, e.g., "+ out" refers to hydrogen supplied whereby the cathode tap is located at the outlet.

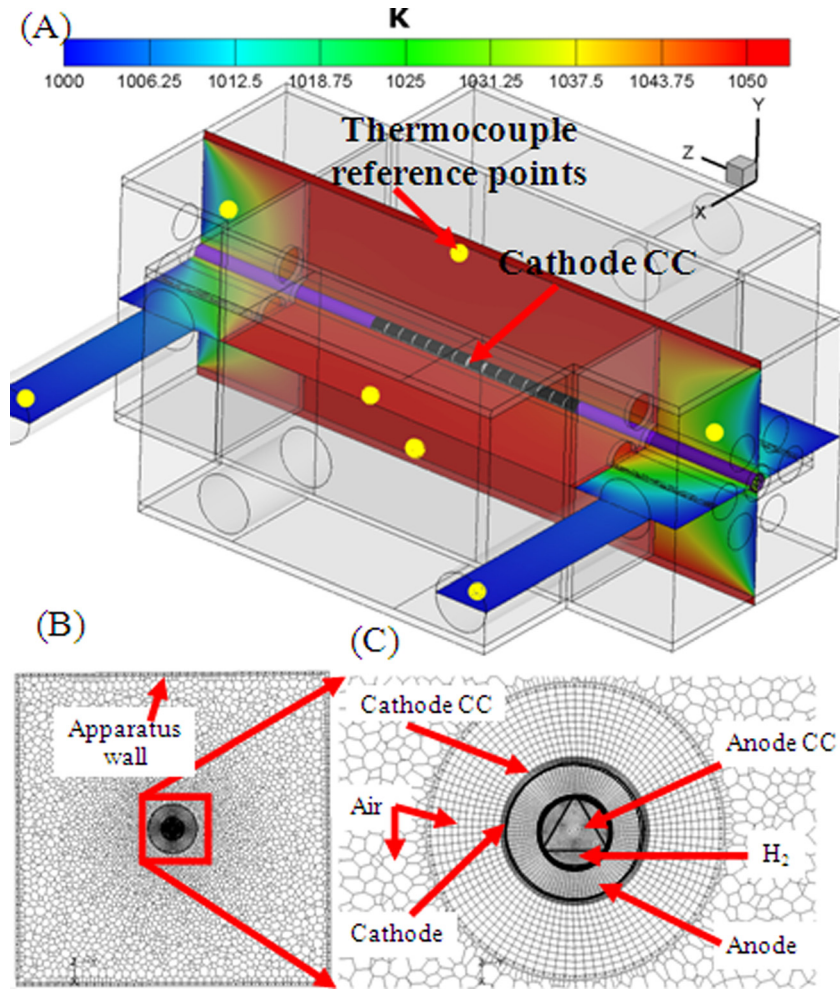


Fig. 3 (a) Temperature profile of apparatus confirmed by thermocouple measurement at locations indicated with a yellow dot, (b) view of meshing on the xy plane and, (c) meshing around the MT-SOFC on the xy plane

ideal case, whereby there was uniform contact between the electrodes and highly conductive current connectors. The electric field, mass species, energy transport, fluid flow, heat transfer, and mass transfer in the manifolds and porous electrodes are all considered. Furthermore, since the electrochemical performance within the SOFC is coupled to the gas flow rate and local temperature, the following standard conservation laws, Eqs. (1)–(3), are used in the model [35]:

Conservation of Mass.

$$\frac{d\rho_i}{dt} + \nabla \cdot \rho_i \vec{v} = S_{m,i} \quad (1)$$

where ρ_i is species density, t is the time, v is the fluid velocity vector, and $S_{m,i}$ is the rate of species i production, attributable to chemical reactions.

Conservation of Momentum.

$$\frac{\partial}{\partial t}(\rho \vec{v}) + \nabla \cdot (\rho \vec{v} \vec{v}) = -\nabla p + \nabla \cdot (\bar{\bar{\tau}}) + \rho \vec{g} + \vec{F} \quad (2)$$

whereby p is the static pressure, $\bar{\bar{\tau}}$ is the stress tensor, and $\rho \vec{g}$ is the gravitational body force vector, respectively. The external body force \vec{F} vector contains other model-dependent source terms such as porous-media sources.

Conservation of Energy.

$$\frac{\partial}{\partial t}(\rho E) + \nabla \cdot (\vec{v}(\rho E + p)) = -\nabla \cdot \left(\sum_i h_i J_i \right) + S_h \quad (3)$$

whereby E is the total energy per unit mass, h is the enthalpy, and J is the diffusive mass flux. The first three terms on the right side of Eq. (3) represent energy transfer due to conduction, species diffusion, and viscous dissipation. At the electrolyte electrode interfaces, S_h includes the heat of chemical reaction and all other volumetric heat sources including SOFC ohmic heat generation.

The energy equation (Eq. (4)) needs treatment at the electrode-electrolyte interface to account for the heat generated or lost as the result of electrochemistry and the overpotentials (i.e., activation overpotential and ohmic loss through the electrolyte). The total energy balance on the electrolyte interface is computed by enumerating the enthalpy flux of all species, including the heat of formation (sources of chemical energy entering the system), and then subtracting off the work done (leaving the system), which is the local voltage jump multiplied by the local current density. What remains is the waste heat due to irreversibilities. S_h in Eq. (4) accounts for the heat of chemical reaction and all other volumetric heat sources. Additionally, in the electrically conducting zones, the SOFC ohmic heat generation is accounted for within this term. In all solid MT-SOFC components, the electric

field solution, including electrode and electrolyte ohmic heating, is accounted for by Eq. (4) [35].

$$\frac{\partial}{\partial t}(\rho E) + \nabla \cdot (\vec{v}(\rho E + p)) = \nabla \cdot \left(k_{\text{eff}} \nabla T - \sum_i h_j \vec{J}_j + (\vec{\tau}_{\text{eff}} \cdot \vec{v}) \right) + S_h \quad (4)$$

Note that k_{eff} is the effective thermal conductivity, the definition of which depends on the flow regime (laminar or turbulent).

The CFD code assumed that the electric field and the electrochemistry interact solely at the electrolyte interface. It treats the electrolyte interface as an impermeable wall consisting of a 1D electrolyte and 2D electrolyte electrode interfaces. Thus, the potential field requires a “jump condition” applied to the two sides of this 1D electrolyte wall in order to account for the electrochemistry effects. This jump condition encapsulates the anode/cathode voltage due to Nernst, the voltage reduction due to activation, the Ohmic loss due to the resistivity of the electrolyte, and a linearized term for the voltage reduction due to activation losses. This interface condition relates the potential on the anode and the cathode side of the electrolyte. It has the following form:

$$\varphi_{\text{jump}} = \varphi_{\text{ideal}} - \eta_{\text{ele}} - \eta_{\text{act,a}} - \eta_{\text{act,c}} - \eta_s \quad (5)$$

$$\eta_{\text{elec}} = \frac{I^*_{\text{ele}}}{\sigma_{\text{elec}}} \quad (6)$$

where η_{ele} is the ohmic over-potential of the electrolyte, $\eta_{\text{act,c}}$ is the cathode over-potential, $\eta_{\text{act,a}}$ is the anode over-potential, φ_{ideal} is the Nernst potential, and η_s is the ohmic loss in the solid conducting regions. The SOFC module uses a Taylor’s series expansion where a previous value for current density i_{old} is used. The Butler–Volmer equation for the activation potential is nonlinear, and this Taylor’s series expansion is used to make a locally linearized form as described in Eqs. (7)–(9).

$$\eta_{\text{act}}(i^*) \approx \eta_o - \eta_1 (i^* - i^*_{\text{old}}) \quad (7)$$

$$\eta_o = \eta_{\text{act}}(i^*_{\text{old}}) \quad (8)$$

$$\eta_1 = - \frac{\partial \eta_{\text{act}}}{\partial i} \Big|_{i^* = i^*_{\text{old}}} \quad (9)$$

Using this approximation, the voltage jump across the electrolyte is formulated as shown in Eq. (10):

$$V \approx \underbrace{[N - \eta_o + \eta_1 i^*_{\text{old}}]}_{\text{constant}} - \underbrace{i^* [\rho^*_{\text{ele}} \cdot i^*_{\text{ele}} + \eta_1]}_{\text{Linear with local identity}} \quad (10)$$

where V is the anode to cathode voltage, N is the Nernst potential, ρ^* is the electrical resistivity, and i^* is the electrolyte thickness. Here, the activation overpotential is included as a direct reduction of the voltage and as an additional effective resistance. To find the activation over potential at the anode and the cathode, the Newton method can be used to solve the full version of the Butler–Volmer Eq. (11) [35]:

$$i^* = i^*_{\text{0eff}} \left[\exp \frac{\alpha_{\text{anode}} m_{\text{act}} F^*}{RT} - \exp \frac{\alpha_{\text{cathode}} m_{\text{act}} F^*}{RT} \right] \quad (11)$$

where

$$\eta_{\text{act}} = (\phi - \phi_0)$$

ϕ_0 = the potential field at the cell centroid.

ϕ = is the ideal cell potential.

where i^* is the current density i^*_{0eff} is the exchange current density, α is the electrode specific transfer coefficient, η_{act} is the acti-

vation polarization, n is the number of electrons transferred per reaction, R is the universal gas constant, T is the absolute temperature, and F^* is Faradays constant. The transfer coefficient is considered to be the fraction of the change in the polarization, which leads to a change in the reaction rate constant. For fuel cells, its value is usually 0.5. The exchange current density is the forward and reverse electrode reaction rate at the equilibrium potential. Exchange current densities describe intrinsic rates of electron transfer between electrodes. Such rates provide structural and electronic insights into these elements (anode and cathode), and in general, the exchange current density depends on the composition of the electrode, the state of the electrode surface (e.g., surface roughness, presence of oxides, adsorbed species on the surface), concentration of the electro-active species in the solution (both the reduced and oxidized form), the composition of the electrolyte, and temperature. High exchange current densities mean a high electrochemical reaction rate and, hence, the possibility of good fuel cell performance [36].

The CFD software calculates the fluid composition at each model grid point. Therefore, the calculation of concentration polarization is inherent in the calculation [37]. The multicomponent diffusion model is used in order to calculate the diffusion coefficient of species i in the mixture j . The effect of porosity on the multi component mass diffusion coefficient is considered in Eq. (12)

$$D_{i,j,\text{eff}} \equiv \frac{\varepsilon}{\tau^*} D_{i,j} \quad (12)$$

where ε is the porosity, τ^* is the tortuosity, and D is the binary diffusion coefficient of species i in mixture j . In order to account for electrical conduction, three-dimensional electrical conduction is directly comparable to the calculation of heat transfer, and the CFD software [34] uses this concept as a means to calculate the electric field. The conservation of charge is the basis for the calculation of the potential field throughout the electrically conducting regions of a model. This is expressed below in Eqs. (13) and (14) [35].

$$\nabla \cdot i^* = 0 \quad (13)$$

where

$$i^* = -(\sigma \nabla \phi) \quad (14)$$

σ is the electrical conductivity, ϕ is the electrical potential, and i^* is the current density.

The redox reactions must be modeled at the electrodes, electrolyte, and gas species interfaces. Using the local electrical current information, the SOFC model applies species fluxes to the electrode boundaries. Therefore, the reactions at the cathode and anode electrodes are considered in Eqs. (15) and (16) [37].

$$S_{\text{O}_2^-} = - \frac{i}{2F} \quad (15)$$

$$S_{\text{H}_2\text{O}} = \frac{i}{2F} \quad (16)$$

For more information regarding the solution procedure and equations, the reader is pointed to documentation from the CFD code provider [35] or from excellent summaries produced by Sleiti [31] or Christman and Jensen [37].

The predictability of this approach has been compared in the thesis of Lawlor [38] and in Lawlor et al. [39] to experimental results, whereby another case Lawlor et al. [40], was used as the experimental setup. These results can be found in Ref. [39]. The results showed that these models under those conditions of Ref. [40] provided adequate accuracy regarding species, temperature, and electrical performance of the MT-SOFC under test. The same electrochemical and MT-SOFC properties were used in this study.

The surface-to-surface (S2S) radiation model was used in order to account for the radiation exchange in the test apparatus enclosure. The energy exchange between two or more surfaces depends, in part, on their size, separation distance, and orientation. These parameters are accounted for by a geometric function called a “view factor.” More information on this topic can be found in Ref. [34]. The main assumption of the S2S model is that any absorption, emission, or scattering of radiation can be ignored; therefore, only “surface-to-surface” radiation need be considered for analysis. This was certainly the case inside the testing apparatus modeled as optical thickness was certainly insignificant.

The S2S radiation model is computationally very expensive when there are a large number of radiating surfaces. Thus, in order to reduce the computational time as well as the storage requirement, the number of radiating surfaces is reduced by creating surface “clusters.” The surface clusters are made by starting from a face and adding its neighbors and their neighbors until a specified number of faces per surface cluster is collected. A value of one cell per cluster was applied on the MT-SOFC cathode side wall and ceramic inlet pipe while a value of four cells per cluster was applied on the test chamber inner housing.

The normalized radiation error is defined as in Eq. (17).

$$E = \frac{\sum (J_{\text{new}} - J_{\text{old}})}{\text{All radiating features}} \quad (17)$$

where the error E is the maximum change in the radiosity J at the present S2S sweep, normalized by the maximum surface emissive power, and N is the total number of radiating surface clusters. The radiation calculation was deemed to be converged when E decreased to 1×10^{-6} or less. For more information regarding the fuel cell solution process and equations, the reader is directed to documents from the CFD code provider [34,35] or to sufficient summaries by Christman and Jensen [37] or Sleiti [31].

3.2 Calculation. A commercially available CFD modeling software [34] with an electrochemical module [35] was used in order to simulate the manifold designs discussed in this paper on MT-SOFC performance. The MT-SOFC dimensions were: anode thickness 85×10^{-5} m, electrolyte thickness 1×10^{-5} m, and cathode thickness 5×10^{-5} m. The MT-SOFC modeled had a 2.7 mm external diameter and a 1 mm internal diameter. The MT-SOFC active area was 2.97×10^{-4} m². For the cross flow case, the flow from the diffuser was assumed to be uniform, and thus the cross flow inlet pipe and chamber before the diffuser, seen in Fig. 1, was neglected. This was done in order to reduce the number of mesh elements required in the simulation and also in order to simplify the radiation calculation.

For momentum, body forces, species, and the SOFC module, the second order upwind discretization scheme was used. The standard discretization scheme was used for pressure. Discretization of the energy terms within the model was considered via a third order discretization “QUICK.” The Reynolds numbers, for the flows both inside and outside the MT-SOFC, can be described as laminar. This was deduced by using a standard calculation and reference to a standard engineering moody diagram for flow inside a pipe and literature available for flow around a cylinder in cross flow [35]. The pressure based solver was used, and the SIMPLE scheme was used for the pressure velocity coupling. A description of the modeling parameters, used in the CFD solving process, can be seen in Table 1. As a reference regarding the other simulation parameters, the reader could follow Ref. [41] with the changes highlighted in Table 1 noted. From several test cases, the convergence of the model was deemed acceptable when the residuals of velocity (x, y , and z) and continuity were below 1×10^{-5} and when the species and energy equations were below 1×10^{-8} . Furthermore, monitors on several features such as MT-SOFC voltage, current, species concentrations on the outlets, and MT-SOFC

Table 1 Detailed modelling parameters. (m) = measured, (f) = fitted, and (c) calculated. *Average value.

Modelling parameters	Value	Units
Electrochemical properties		
Cathode exchange current density	1000	A/m ² (f)
Anode exchange current density	17,500	A/m ² (f)
Electrolyte resistivity	0.5	ohm·m [41]
Electrical Properties		
Anode conductivity	6,000,000	1/ohm·m (m)
Cathode conductivity*	800	1/ohm·m (m)
Nickel and silver conductivity	1.50×10^7	1/ohm·m [41]
Silver touch cathode resistance	6×10^{-4}	ohm·m ² (c)
Nickel touch anode resistance	1×10^{-6}	ohm·m ² (c)
Anode properties		
Density	3310	kg/m ³ [42]
Cp	430	J/kg·K [42]
Thermal conductivity	1.86	W/m·K
Porosity	0.3	[41,43,44]
Cathode properties		
Density	3030	kg/m ³ [42]
Cp	470	J/kg·K [42]
Thermal conductivity	2.16	W/m·K [42]
Porosity	0.3	[41,43,44]
Current collector properties		
Density	8900	kg/m ³ [41]
Cp	446	J/kg·K [41]
Thermal conductivity	72	W/m·K [41]
Porosity	0.75	(f)

temperature were all analyzed before a realistic solution was accepted.

Additionally, during initial test cases various grids were used in order to adjudicate grid independence of the solution. Indeed, in order to account for the silver mesh on the cathode, the model contained more than an adequate amount of mesh elements in the fluid zones close to the MT-SOFC. The reader is pointed to Ref. [39] for reference to a grid analysis study for modeling similar MT-SOFCs. The model had at total of 7.5 M nodes and contained fully conformal hexahedral and polyhedral mesh elements. Figure 3(a) shows the experimental apparatus test case whereby measurements were made with several thermocouples located by the yellow dots. These measurements were used to fine tune, via radiation parameters, the model apparatus temperature profile. Note that the values for emissivity on the MT-SOFC wall were obtained from Ref. [45], where the effect of silver was ignored and the emissivity’s on the proposed testing apparatus housing were fitted as 0.55. The Anode and cathode exchange current densities were fitted. These values were estimated by simply using trial and error. The state of the art problems associated with defining exchange current density and then even modeling exchange current density values has been discussed in Refs. [36,46,47]. As the goal of this study was to study the effect on MT-SOFC performance as a function of flow regimes, these exchange current density values were not investigated further. Furthermore, the measured maximum 20 °C change in MT-SOFC temperature, considering an H₂/H₂O mix, would have negligible effect on the exchange current density temperature dependence on the I/V curves predicted by the model [43]. This is furthermore substantiated by our current results, the previous results in Ref. [39], and indeed the works of others using similar software and fitting procedure [31,32,48–50].

Figures 3(b) and 3(c) show a sample of the numerical grid on the xy plane. The difficulty in modeling these MT-SOFCs was the small thickness of the cathode (50 μm), which required about five cells in order to account accurately for heat transfer through the electrode. Furthermore, the grid size change and aspect ratio changes were kept to a minimum, below 5. The silver wires on the

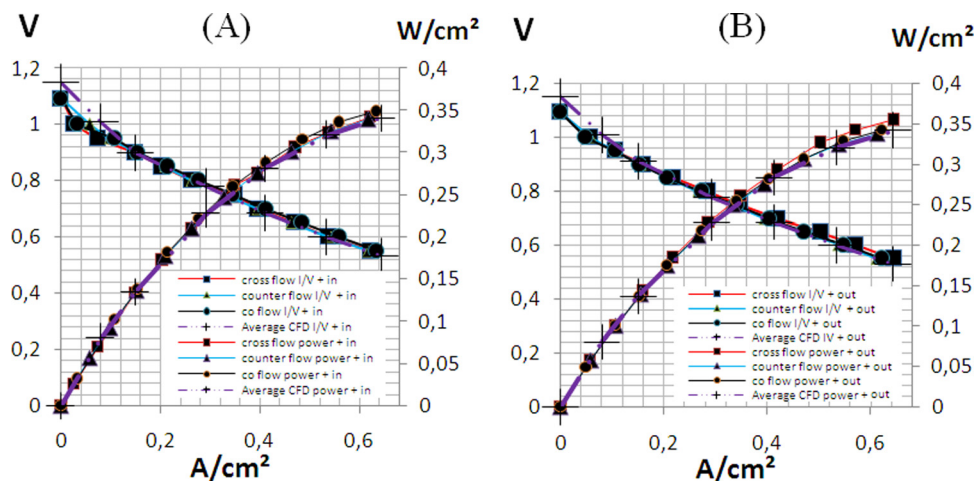


Fig. 4 I/V and power curve showing simulated and measured recordings when the cathode tap was located at the fuel inlet “+ in” (a) and outlet “+ out” (b)

cathode current collector, see “cathode CC” in Fig. 3, also proved a challenge to include, as they were extremely thin zones and were meshed three cells deep. The “Gambit” [34] meshing tool was used to manually generate the model mesh.

4 Results and Discussions

A comparison of the MT-SOFC I/V curves, measured in the experimental apparatus under all three manifold conditions and both cathode current collection positions is shown in Figs. 4(a) “+ in” and 4(b) “+ out.” Please refer to Fig. 2 in order to establish these “+” terminologies. The oxidant flow regime was compressor air, and it was regulated by a flow controller to 105 ml_N/min. The fuel flow was 50 ml_N/min of 97 mol. % H₂ and 3 mol. % H₂O. Since so many plots would be required should every simulation predicted I/V curve also be shown, the averaged CFD predicted result is shown. The variation between the CFD simulated plots was quite small with a less than 3% difference between the largest and smallest power value predicted at 0.55 V. More variation was observed in the measured data as can be seen in Figs. 4(a) and 4(b), up to a maximum of 8% variation in power measurements at 0.62 A/cm². This measurement variation can almost certainly be attributed to the small temperature fluctuations that were caused by the “on/off” PID controlled heating system. This statement is furthermore substantiated by the fact that no clear electrical property trends between similar regimes were observed in Figs. 4(a) and 4(b). Clearly, the flow regime had no noticeable effect on the MT-SOFC electrical performance, and furthermore, the cathode current collector location in relation to the MT-SOFC fuel inlet had no noticeable effect. This latter fact meant that the rather low fuel utilization 28%, combined with the ample silver current collection on the cathode, allowed for a very effective MT-SOFC current generation and collection system, albeit, at the cost of fuel utilization and plenty of silver wire and paste.

A significant 5.2% variation between the CFD predicted OCV and measured OCV can be observed in both Figs. 4(a) and 4(b). This may have been caused by small short circuits in the electrolyte, although the stability of the measured OCV remained relatively constant through the measurements and no temperature variation was measured upon changing from a 95/5 mol. % N₂/H₂ to 100 mol. % H₂ mix. Activation losses, ohmic losses, or indeed mass transport losses that were not accounted for by the CFD simulation seem more likely to be the cause of this OCV difference.

Figures 5(a)–5(c) depict each of the three thermocouple measurements recorded at positions on the MT-SOFC cathode. Apart from the nonconformal reading on “cathode mid + in” at 0.35 A/cm², the largest deviation between two measurements recorded at any

current density was 2.6 K, which was accounted for by the temperature fluctuation caused by the apparatus heating system on the measurement. Furthermore, an averaged CFD temperature prediction at the thermocouple location for all three cases is included in Figs. 5(a)–5(c). It was experimentally measured and predicted via CFD modeling that the flow regime had negligible effect on the MT-SOFC temperature distribution. In fact, the CFD predictions showed insignificant deviations (< 0.5%) between each predicted regime power curve point predictions. Also Fig. 5(d) shows a comparison of the measured MT-SOFC current density for the three manifold regimes under various oxidant flow rates when the cathode current tap was located at the hydrogen exhaust “out +.” The measurements and CFD prediction show that the oxidant flow rate as a function of the three different manifold techniques had little effect on the MT-SOFC electrical performance.

In Fig. 5(d), an averaged CFD model prediction showed an MT-SOFC electrical performance similar to the measured cases for all oxidant flow rates. The maximum difference between any two measured current density recordings was 0.06 A/cm² meaning a 12% measurement variation, and the maximum difference between any measured value and the averaged simulation prediction was 0.05 A/cm² meaning a 10% measurement variation. The cross-flow case, at lower oxidant flow rates, caused slightly lower MT-SOFC current densities compared to the co- and counter-flow cases. The CFD predictions also showed a similar trend, but the deviation between the co/counter- and cross-flow measurement was, at 42 ml_N/min, 3.2% compared to 16% for the measured values. The average velocity (inside the apparatus) attributed to a 42 ml_N/min flow in the cross flow case was predicted to be about 1 mm/s as compared to 2.3 mm/s in the cross- and co-flow cases. Neglected, buoyant flows or nonuniform flows etc. associated with such low velocities in the cross flow case may have occurred in the experimental apparatus that were not accounted for in the numerical simulation. This point requires further investigation, but such an effect on the current density as a function of the flow regime and its velocity will surely be much easier to establish in the seven MT-SOFC experiments and simulations.

While the thermocouple measurements and simulation predictions shown in Fig. 5 provide an interesting account of the temperature profiles on the MT-SOFC cathode, CFD can be used in order to fill in “phenomena” gradient gaps using contour plots. The assumption was that the thermocouple readings and current density readings are sufficient validation parameters for such simulations. Figure 6(a) shows the predicted temperature profile on the MT-SOFC cathode for the co-flow case. In all the following contour plots, the cathode current tap was located at the top of the

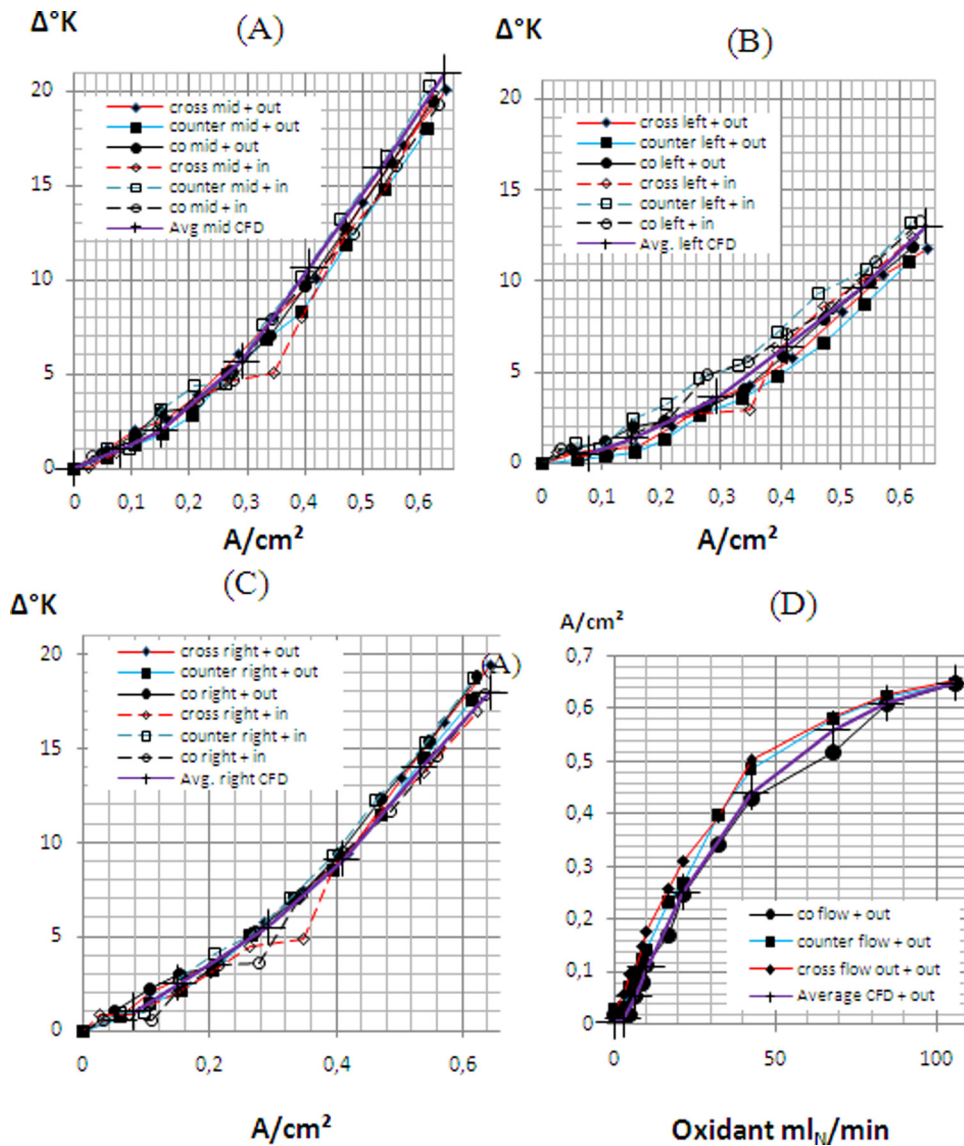


Fig. 5 Temperature measurements and averaged CFD temperature prediction for all manifolds at (a) the middle thermocouple position, (b) left thermocouple position, (c) right thermocouple position (refer to Fig. 2). (d) The recorded and CFD predicted MT-SOFC current density as a function of oxidant inlet flow rate.

MT-SOFC. When comparing Fig. 6(a) “+ out” with Fig. 6(c) “+ in,” it can be seen that the temperature profiles are very similar, whereby the hottest part of the MT-SOFC was located just above the MT-SOFC center.

The top part of the MT-SOFC, in comparison to the bottom part, was always hotter. This is in spite of the various oxidant and fuel flow regimes. As seen in Figs. 6(b) and 6(d), the cathode current tap location, in relation to the hydrogen inlet, had a much more pronounced effect on the MT-SOFC current density profile. The red arrows in Figs. 6(b) and 6(d) show the location of the fuel outlet, while the black arrow indicates the oxidant flow direction. In the case where the fuel inlet was at the same location as the cathode current tap (Fig. 6(d)), the current density distribution across the MT-SOFC tended to show higher current density values near the current tap/hydrogen inlet. In comparison, in Fig. 6(b), where the hydrogen inlet was opposite the cathode current tap, the current density distribution was slightly more homogenous, especially in regions not covered by the silver current collector. High current density rings and line zones, where the current collector was located, can quite clearly be seen on the cathode as zones of higher current density.

The relatively low fuel utilization, 28% in this case, is almost certainly the reason for the rather homogeneous current production along the MT-SOFC. The zones of lower current production (blue spots on the cell, refer Figs. 6(b) and 6(d)), correspond to the cathode zones that did not have a current collector placed over them. This is an indication of how important adequate current collection on the cathode is. The zones not directly covered by the cathode current collector experienced at worst a factor two lower current density when compared to the zones of maximum current density. This phenomenon is likely a function of the distance from the current collector. Figures 6(b) and 6(d) show the oxidant species concentration in mole percent as a function of fuel inlet and outlet. It can be seen that the oxidant is not being refreshed to the chamber at an optimum rate, as the amount of oxidant even entering the testing chamber is 10% lower than terrestrial conditions. This was caused by the design of the testing apparatus and the very low flow rates.

Figures 7(a) and 7(c) show temperature plots, which were predicted by the CFD software, for the counter-flow regime. When these plots are compared with Figs. 6(a) and 6(c), it can be seen that the oxidant flow regime had negligible effect on the MT-SOFC

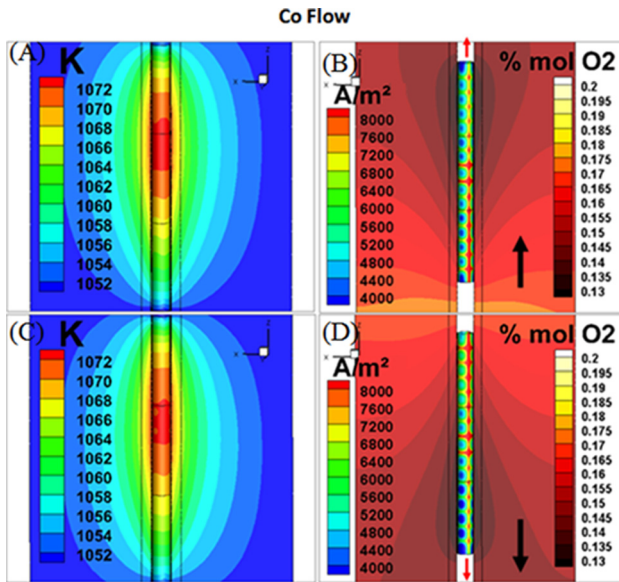


Fig. 6 Co-flow temperature, species, and current density plots for (a) and (b) “+ out” and (c) and (d) “+ in”

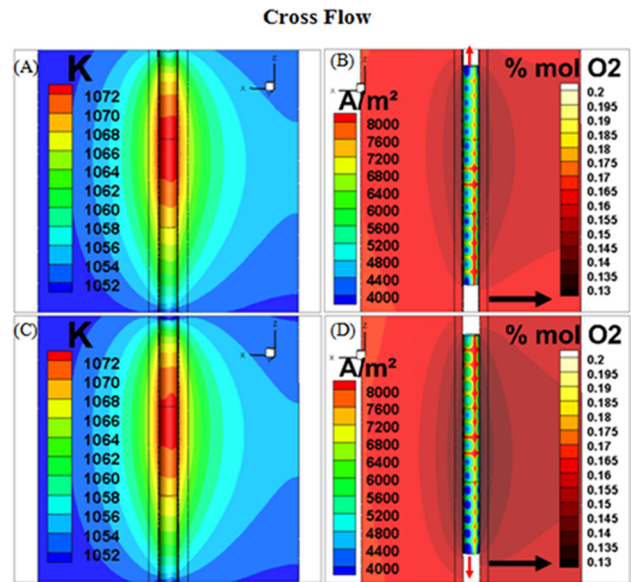


Fig. 8 Cross-flow temperature, species, and current density plots for (a) and (b) “+ out” and (c) and (d) “+ in”

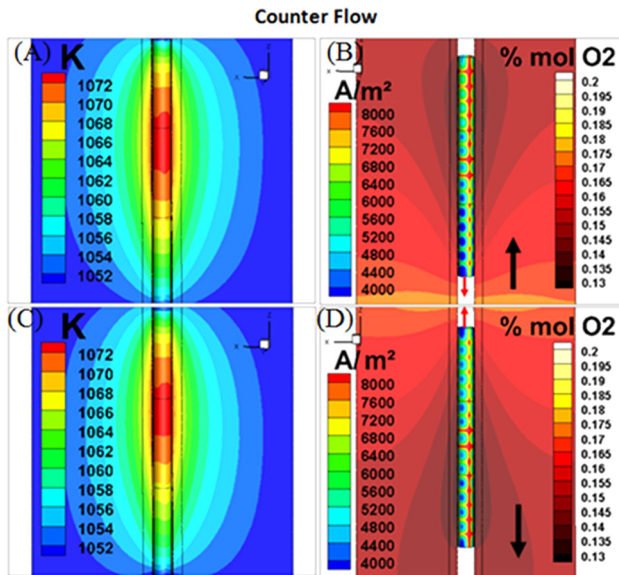


Fig. 7 Counter-flow temperature, species, and current density plots for (a) and (b) “+ out” and (c) and (d) “+ in”

temperature profile. Figures 7(b) and 7(d) show the species concentration distribution as a function of the cathode current tap location in relation to the hydrogen inlet. The oxidant species concentrations are opposite in form in Figs. 7(b) and 7(d) as the hydrogen flow is in the opposite direction. Where the hydrogen was supplied, the current density was the highest similar to the co-flow case; refer to Figs. 6(b) and 6(d). It was expected that the counter-flow regime would have produced a lower maximum current density and lower minimum O_2 mole percent distribution as the depletion of the oxygen along the MT-SOFC should, in this regime, be most pronounced at the hydrogen inlet. However, this effect was not noticed in these CFD predictions, and indeed this effect was not observed in the I/V measurements; please refer to Fig. 4.

The cross-flow case, seen in Fig. 8, also continued the trend seen in Figs. 6 and 7 whereby the temperature plots in Figs. 8(a) and 8(c) were unaffected by the flow regime. A perhaps interesting difference was observed in the species concentration plots

seen in Fig. 8 where the variation of the species mole fraction was substantially less than in Fig. 6 and Figs. 7(b) and 7(d). This was because the oxygen depletion along the MT-SOFC length (i.e., co- and counter-flow) had a larger effect in causing the lower oxygen species concentration than oxygen depletion along the MT-SOFC diameter (i.e., cross-flow). An interesting CFD prediction was that the oxidant species distribution minimum was predicted to be 5.4% lower in the co- and counter-flow case when compared with the cross flow case. This was in spite of average velocity attributed to a 105 ml_N flow in the cross flow case was 2.4 mm/s as compared to 4.6 mm/s in the co- and cross-flow cases. At these low velocities, the oxygen diffusivity had a significant impact whereby the longer flow path in the co- and counter-flow cases had an effect.

Regardless of the temperature distribution and current density distribution in Figs. 8(a)–8(d) were the same as observed in Fig. 6 and Figs. 7(a)–7(d) showing that the fuel inlet and current collector position had more effect on the MT-SOFC performance than oxidant flow regime. For all three oxidant flow regimes, it was observed that when the fuel was supplied at the same position as the current tap (Figs. 6(b), 7(b), and 8(b)), there was a large current density distribution across the MT-SOFC when compared to the case whereby the current tap was located at the fuel outlet (Figs. 6(d), 7(d), and 8(d)). However, in both situations, regardless of oxygen regime, the MT-SOFC produced exactly the same amount of power. In order to produce almost identical average power densities for each case, this meant that the higher current density at the MT-SOFC inlet and lower current density at the outlet, for the case where the cathode current tap was located at the fuel inlet (Figs. 6(b), 7(b), and 8(b)) was compensated for by the slightly more uniform current distribution in the case where the cathode current collector was located at the fuel outlet (Figs. 6(d), 7(d), and 8(d)).

5 Conclusions and Outlook

In all three cases, co-, counter-, and cross-flow, the flow regime had no observable impact on the MT-SOFC electrical performance or temperature profile with an oxidant flow rate of 105 ml_N/min. This fact was both experimentally measured and numerically simulated. Exactly why the temperature profile that was measured using thermocouples and subsequently predicted by the CFD code was always hottest just above the MT-SOFC center is not clear and requires further investigation. In our previous thermograph

measurements [40] and CFD predictions [39], the maximum temperature was closer to the hydrogen inlet. However, the cathode current collector location in this case was located at the MT-SOFC center, and the current collector distribution on the MT-SOFC cathode was much less, which may be an explanation for the discontinuity in results. Moreover the cell tested in Ref. [40] was from a different generation with properties that allowed a much higher electrical performance.

If the hydrogen concentration was the cause of this higher temperature at the inlet in Ref. [40], then the results of the current study should also have shown this trend. In fact, this study has shown that while most of the electricity was generated in regions close to the hydrogen inlet, this is not necessarily true of cathode side heat generation. Apart from the slightly higher “lowest mole percent oxygen CFD prediction,” there was little variation in other phenomena between the three manifold techniques. What exactly the results of the single MT-SOFC measurements and CFD predictions mean for a MT-SOFC stack is unclear. This is because of the altered radiation properties of a bundle in the apparatus and higher oxidant flow rates in comparison to the single MT-SOFC case. It is expected that the MT-SOFC in the middle of the seven cell bundle we have designed will become substantially hotter. It will be interesting to see the effect of neighboring MT-SOFCs on the center MT-SOFC temperature and indeed its surrounding species concentration. These effects will surely be a function of the MT-SOFC to MT-SOFC spacing, which may be rather easily optimized using CFD. The apparatus used in these experiments was designed to hold a seven MT-SOFC stack, and measurements and CFD simulation will be performed again in the future.

In a further study, different fuel compositions and inserting thermocouples inside the anode are also being considered.

Acknowledgment

This work is being funded by the Austrian Science fund, Fonds zur Förderung der Wissenschaftlichen Forschung (FWF), under the project title HIT-SIM (Project No. L611-N14), which is gratefully acknowledged.

Nomenclature

ρ^*	= electrical resistance, ohm
i^*	= current density, A/m ²
t^*	= thickness, m
Ω	= resistance, ohm
N	= Nernst potential, V
η_{act}	= activation loss, V
η_{ohm}	= ohmic loss, V
η_{con}	= concentration loss, V
j	= species
ρ	= density kg/m ³
v	= velocity m/s
\bar{t}	= stress tensor, N/m ²
g	= gravity, m/s ²
p	= pressure, pa
t	= time, s
T	= temperature, K
H	= enthalpy, J
E	= total energy per mass, J/kg
$Sm_{,j}$	= species j sink/source, kg/s
S_h	= volumetric heat source, J/m ³
K_{eff}	= effective conductivity, W/mK
Φ	= ideal cell potential, V
Φ_0	= potential at cell centroid, V
i^*_0	= exchange current density, A/m ²
α	= transfer coefficient
n	= number of electrons 2
F^*	= Faradays constant 96,485.3399 C mol ⁻¹
R	= universal gas constant 8.3145, J/mol K
J	= diffusive mass flux kg/s m ²

$D_{i,j}$ = binary diffusivity of a species i into species j , m² s⁻¹
 σ_{ele} = electrolyte conductivity, S/m

References

- [1] Badwal, S. P. S., and Foger, K., 1996, “Solid Oxide Electrolyte Fuel Cell Review,” *Ceram. Int.*, **22**(3), pp. 257–265.
- [2] Payne, R., Love, J., and Kah, M., 2009, “Generating Electricity at 60% Electrical Efficiency from 1–2 kW SOFC Products,” *ECS Trans.*, **25**(2), pp. 231–239.
- [3] Chan, S. H., Ho, H. K., and Tian, Y., 2003, “Multi-Level Modeling of SOFC-Gas Turbine Hybrid System,” *Int. J. Hydrogen Energy*, **28**(8), pp. 889–900.
- [4] Calise, F., Dentice D’Accadia, M., Palombo, A., and Vanoli, L., 2006, “Simulation and Exergy Analysis of a Hybrid Solid Oxide Fuel Cell (SOFC)-Gas Turbine System,” *Energy*, **31**(15), pp. 3278–3299.
- [5] Cocco, D., and Tola, V., 2009, “Externally Reformed Solid Oxide Fuel Cell-Micro-Gas Turbine (SOFC-MGT) Hybrid Systems Fueled by Methanol and Di-Methyl-Ether (DME),” *Energy*, **34**(12), pp. 2124–2130.
- [6] Kandepu, R., Imsland, L., Foss, B. A., Stiller, C., Thorud, B., and Bolland, O., 2007, “Modeling and Control of a SOFC-GT-Based Autonomous Power System,” *Energy*, **32**(4), pp. 406–417.
- [7] Calise, F., Dentice D’Accadia, M., Vanoli, L., and Von Spakovsky, M. R., 2007, “Full Load Synthesis/Design Optimization of a Hybrid SOFC-GT Power Plant,” *Energy*, **32**(4), pp. 446–458.
- [8] Komatsu, Y., Kimijima, S., and Szymid, J. S., 2010, “Performance Analysis for the Part-Load Operation of a Solid Oxide Fuel Cell-Micro Gas Turbine Hybrid System,” *Energy*, **35**(2), pp. 982–988.
- [9] Burer, M., Tanaka, K., Favrat, D., and Yamada, K., 2003, “Multi-Criteria Optimization of a District Cogeneration Plant Integrating a Solid Oxide Fuel Cell-Gas Turbine Combined Cycle, Heat Pumps and Chillers,” *Energy*, **28**(6), pp. 497–518.
- [10] Santin, M., Traverso, A., Magistri, L., and Massardo, A., 2010, “Thermoeconomic Analysis of SOFC-GT Hybrid Systems Fed by Liquid Fuels,” *Energy*, **35**(2), pp. 1077–1083.
- [11] Sidwell, R. W., and Coors, W. G., 2005, “Large Limits of Electrical Efficiency in Hydrocarbon Fueled SOFCs,” *J. Power Sources*, **143**(1–2), pp. 166–172.
- [12] Kurachi, S., Mizutani, Y., Hiroyama, T., Katsurayama, K., Okada, F., and Ukai, K., 2009, “Development of a Small-Scale Solid Oxide Fuel Cell (SOFC),” 24th World Gas Conference, Buenos Aires, Argentina, October 5–9, available at <http://www.igu.org/html/wgc2009/papers/docs/wgcFinal00379.pdf>, accessed December 29, 2012.
- [13] Howe, K. S., Thompson, G. J., and Kendall, K., 2011, “Micro-Tubular Solid Oxide Fuel Cells and Stacks,” *J. Power Sources*, **196**(4), pp. 1677–1686.
- [14] Wakui, T., Yokoyama, R., and Shimizu, K.-I., 2010, “Suitable Operational Strategy for Power Interchange Operation Using Multiple Residential SOFC (Solid Oxide Fuel Cell) Cogeneration Systems,” *Energy*, **35**(2), pp. 740–750.
- [15] Ghosh, S., and De, S., 2006, “Energy Analysis of a Cogeneration Plant Using Coal Gasification and Solid Oxide Fuel Cell,” *Energy*, **31**(2–3), pp. 345–363.
- [16] Bujalski, W., Dikwal, C. M., and Kendall, K., 2007, “Cycling of Three Solid Oxide Fuel Cell Types,” *J. Power Sources*, **171**(1), pp. 96–100.
- [17] Alston, T., Kendall, K., Palin, M., Prica, M., and Windibank, P., 1998, “A 1000-Cell SOFC Reactor for Domestic Cogeneration,” *J. Power Sources*, **71**(1–2), pp. 271–274.
- [18] Yamaguchi, T., Suzuki, T., Fujishiro, Y., Awano, M., and Shimizu, S., 2010, “Novel Electrode-Supported Honeycomb Solid Oxide Fuel Cell: Design and Fabrication,” *J. Fuel Cell Sci. Technol.*, **7**(4), p. 041001.
- [19] Yamaguchi, T., Shimizu, S., Suzuki, T., Fujishiro, Y., and Awano, M., 2009, “Evaluation of Extruded Cathode Honeycomb Monolith-Supported SOFC Under Rapid Start-Up Operation,” *Electrochim. Acta*, **54**(5), pp. 1478–1482.
- [20] Lin, P.-H., and Hong, C.-W., 2009, “Cold Start Dynamics and Temperature Sliding Observer Design of an Automotive SOFC APU,” *J. Power Sources*, **187**(2), pp. 517–526.
- [21] Aguiar, P., Brett, D. J. L., and Brandon, N. P., 2007, “Feasibility Study and Techno-Economic Analysis of an SOFC/Battery Hybrid System for Vehicle Applications,” *J. Power Sources*, **171**(1), pp. 186–197.
- [22] Du, Y., Finnerty, C., and Jiang, J., 2008, “Thermal Stability of Portable Micro-tubular SOFCs and Stacks,” *J. Electrochem. Soc.*, **155**(9), pp. B972–B977.
- [23] Penner, S. S., Appleby, A. J., Baker, B. S., Bates, J. L., Buss, L. B., Dollard, W. J., Fartis, P. J., Gillis, E. A., Gunsher, J. A., Khandkar, A., Krumpelt, M., O’Sullivan, J. B., Runte, G., Savinell, R. F., Selman, J. R., Shores, D. A., and Tarman, P., 1995, “Commercialization of Fuel Cells,” *Energy*, **20**(5), pp. 331–470.
- [24] Lutsey, N., Brodrick, C.-J., and Lipman, T., 2007, “Analysis of Potential Fuel Consumption and Emissions Reductions From Fuel Cell Auxiliary Power Units (APUs) in Long-Haul Trucks,” *Energy*, **32**(12), pp. 2428–2438.
- [25] Maru, H. C., Singhal, S. C., Stone, C., and Wheeler, D., 2010, “1–10 kW Stationary Combined Heat and Power Systems Status and Technical Potential,” National Renewable Energy Laboratory, Golden, CO, Report No. NREL/BK-6A10-48265, available at <http://www.nrel.gov/docs/fy11osti/48265.pdf>, accessed December 29, 2012.
- [26] Lawlor, V., Griesser, S., Buchinger, G., Olabi, A. G., Cordiner, S., and Meissner, D., 2009, “Review of the Micro-Tubular Solid Oxide Fuel Cell: Part I. Stack Design Issues and Research Activities,” *J. Power Sources*, **193**(2), pp. 387–399.
- [27] Kendall, K., 2009, “Progress in Microtubular Solid Oxide Fuel Cells,” *Int. J. Appl. Ceram. Technol.*, **7**(1), pp. 1–9.
- [28] Kendall, K., 2005, “Progress in Solid Oxide Fuel Cell Materials,” *Int. Mater. Rev.*, **50**(5), pp. 257–264.

- [29] Recknagle, K. P., Williford, R. E., Chick, L. A., Rector, D. R., and Khaleel, M. A., 2003, "Three-Dimensional Thermo-Fluid Electrochemical Modeling of Planar SOFC Stacks," *J. Power Sources*, **113**(1), pp. 109–114.
- [30] Serincan, M. F., Pasaogullari, U., and Sammes, N. M., 2008, "Computational Thermal-Fluid Analysis of a Microtubular Solid Oxide Fuel Cell," *J. Electrochem. Soc.*, **55**(11), pp. B1117–B1127.
- [31] Sleiti, A. K., 2010, "Performance of Tubular Solid Oxide Fuel Cell at Reduced Temperature and Cathode Porosity," *J. Power Sources*, **195**(17), pp. 5719–5725.
- [32] Cordiner, S., Mariani, A., and Mulone, V., 2010, "CFD-Based Design of Microtubular Solid Oxide Fuel Cells," *J. Heat Transfer*, **132**(6), p. 062801.
- [33] Sciacovelli, A., and Verda, V., 2009, "Entropy Generation Analysis in a Monolithic-Type Solid Oxide Fuel Cell (SOFC)," *Energy*, **34**(7), pp. 850–865.
- [34] ANSYS, 2006, *Fluent 6.3 User's Guide*, Fluent Inc., Canonsburg, PA.
- [35] ANSYS, 2009, *Fluent CFD User Manual: Chapter 3 SOFC Model Theory*, Fluent Inc., Canonsburg, PA.
- [36] Noren, D. A., and Hoffman, M. A., 2005, "Clarifying the Butler–Volmer Equation and Related Approximations for Calculating Activation Losses in Solid Oxide Fuel Cell Models," *J. Power Sources*, **152**, pp. 175–181.
- [37] Christman, K. L., and Jensen, M. K., 2011, "Solid Oxide Fuel Cell Performance With Cross-Flow Roughness," *ASME J. Fuel Cell Sci. Technol.*, **8**(2), p. 024501.
- [38] Lawlor, V., 2010, "Study to Characterise the Performance of MT-SOFCs by the Invention of an Avant Garde Experimental Apparatus and Computational Modelling," Ph.D. thesis, Dublin City University, Dublin, Ireland.
- [39] Lawlor, V., Hochenauer, C., Griesser, S., Zauner, G., Buchinger, G., Meissner, D., Olabi, A. G., Klein, K., Kuehn, S., Cordiner, S., and Mariani, A., 2011, "The Use of a High Temperature Wind Tunnel for MT-SOFC Testing—Part II: Use of Computational Fluid Dynamics Software in Order to Study Previous Measurements," *ASME J. Fuel Cell Sci. Technol.*, **8**(6), p. 061019.
- [40] Lawlor, V., Zauner, G., Hochenauer, C., Mariani, A., Griesser, S., Carton, J. G., Klein, K., Kuehn, S., Olabi, A. G., Cordiner, S., Meissner, D., and Buchinger, G., 2010, "The Use of a High Temperature Wind Tunnel for MT-SOFC Testing—Part I: Detailed Experimental Temperature Measurement of an MT-SOFC Using an Avant-Garde High Temperature Wind Tunnel and Various Measurement Techniques," *ASME J. Fuel Cell Sci. Technol.*, **7**(6), p. 061016.
- [41] ANSYS, 2006, *Fluent 6.3 SOFC Model Tutorial*, Fluent Inc. (Tutorial Series), Canonsburg, PA.
- [42] Cui, D., and Cheng, M., 2009, "Thermal Stress Modeling of Anode Supported Micro-Tubular Solid Oxide Fuel Cell," *J. Power Sources*, **192**(2), pp. 400–407.
- [43] Ni, M., Leung, M. K. H., and Leung, D. Y. C., 2007, "Parametric Study of Solid Oxide Fuel Cell Performance," *Energy Convers. Manage.*, **48**(5), pp. 1525–1535.
- [44] Ni, M., Leung, M. K. H., and Leung, D. Y. C., 2007, "Micro-Scale Modelling of Solid Oxide Fuel Cells With Micro-Structurally Graded Electrodes," *J. Power Sources*, **168**(2), pp. 369–378.
- [45] Lawlor, V., Zauner, G., Mariani, A., Hochenauer, C., Griesser, S., Carton, J., Kuehn, S., Klein, K., Meissner, D., Olabi, A. G., Cordiner, S., and Buchinger, G., 2009, "A Study to Investigate Methods to Measure the Temperature of a MT-SOFC in a High Temperature Wind Tunnel," Proceedings of EFC2009, Rome, Italy, December 15–18, pp. 76–77.
- [46] Andersson, M., Yuan, J., and Sundén, B., 2010, "Review on Modeling Development for Multiscale Chemical Reactions Coupled Transport Phenomena in Solid Oxide Fuel Cells," *Appl. Energy*, **87**(5), pp. 1461–1476.
- [47] Zhu, H., and Kee, R. J., 2003, "A General Mathematical Model for Analyzing the Performance of Fuel-Cell Membrane-Electrode Assemblies," *J. Power Sources*, **117**(1–2), pp. 61–74.
- [48] Prinkey, M., Gemmen, R., and Rogers, W., 2001, "Application of a New CFD Analysis Tool for SOFC Technology," Proceedings of IMECE, New York, November 11–16, pp. 291–300.
- [49] Serincan, M. F., Pasaogullari, U., and Sammes, N. M., 2009, "Effects of Operating Conditions on the Performance of a Micro-Tubular Solid Oxide Fuel Cell (SOFC)," *J. Power Sources*, **192**(2), pp. 414–422.
- [50] Qu, Z., Aravind, P. V., Boksteen, S. Z., Dekker, N. J. J., Janssen, A. H. H., Woudstra, N., and Verkooyen, A. H. M., 2011, "Three-Dimensional Computational Fluid Dynamics Modeling of Anode-Supported Planar SOFC," *Int. J. Hydrogen Energy*, **36**(16), pp. 10209–10220.